RESEARCH ARTICLE
SOLID EARTH: GEOMAGNETISM

Earth and Planetary Physics
9: 635–641, 2025
doi: 10.26464/epp2025060

The magnetic stripe signatures of the North Atlantic Ocean crust derived from *Swarm* and Macau Science Satellite-1 observations

PengFei Liu[1*], Liang Yin[1*], ShiDa Sun[2], and HongBo Yao[1]

[1]Macau Institute of Space Technology and Application, Macau University of Science and Technology, Macao 999078, China;

[2]Key Laboratory of Intelligent Detection and Equipment for Underground Space of Beijing-Tianjin-Hebei Urban Agglomeration, Ministry of Natural Resources, Hebei GEO University, Shijiazhuang 050031, China

Key Points:

- Low-inclination Macau Science Satellite-1 observations are capable of capturing signatures originated from seafloor magnetic stripes.
- The observed amplitudes of the crustal radial magnetic field at 450 km altitude over the North Atlantic Ocean are between −11 nT and +8 nT.
- Low-altitude observation is required for reconstructing fine structures of oceanic magnetic stripes.

Citation: Liu, P. F., Yin, L., Sun, S. D., and Yao, H. B. (2025). The magnetic stripe signatures of the North Atlantic Ocean crust derived from *Swarm* and Macau Science Satellite-1 observations. *Earth Planet. Phys.*, *9*(3), 635–641. http://doi.org/10.26464/epp2025060

Abstract: The Earth's crust, the outer shell of the Earth, consists of continental crust and oceanic crust. Oceanic crust is created at the mid-oceanic ridge, where it is magnetized in the ambient field of the Earth. As new material is extruded, the crust spreads outward, retaining its magnetization. The reversal of the polarity of the Earth's magnetic field over geologic time leads to a pattern of striped magnetic anomalies. In this study, we carry out a preliminary evaluation on how data from the Macau Science Satellite-1 (MSS-1), which has a low orbital inclination, influences inversion models of the oceanic crustal magnetic field when combined with data from the *Swarm* mission. For our modeling we use an equivalent source method based on a cubed-sphere grid. Our model captures the broad magnetic structure over the North Atlantic Ocean and demonstrates that the trend of magnetic stripes is consistent with the age frame of the oceanic crust. The amplitude of the radial magnetic field at 450 km the North Atlantic Ocean ranges from −11 nT to +8 nT. The addition of MSS-1 observations to *Swarm* data generates results consistent with the overall magnetic stripe pattern. The lack of short-wavelength scale structure reveals the limitation of high-altitude satellites in portraying fine features and hence lower-altitude observations would be required to delineate a more detailed crustal signature. It is expected to obtain a finer structure of oceanic magnetic stripes by combining low-altitude CHAMP field data and east–west gradient data derived from MSS-1 in future work.

Keywords: ocean magnetic stripes; lithospheric magnetic structure; Macau Science Satellite-1

1. Introduction

Satellite magnetic observations are crucial to improve the accuracy of our knowledge of the large-scale magnetic field of the Earth (Ebbing et al., 2021). Systematic measurement of the field by satellite observation began with the Polar Orbiting Geophysical Observatory (POGO) series (1964 to 1972); following POGO was the MAGSAT mission (1979 to 1980). The Danish Oersted mission in 2000 ushered in the modern era of satellite observations of the Earth's magnetic field (Sabaka et al., 2020). Oersted had a near-polar orbital (96.5°) at an elevation between 630–860 km above the Earth's surface. The CHAMP mission (2000–2010) had an orbital inclination (angle between satellite orbit and equator) of 87.3°and orbited at an altitude of 250–450 km. Both Oersted and CHAMP were equipped with a scalar magnetometer with 0.5 nT accuracy and a vector fluxgate magnetometer (VFM); the resolution of Oersted's VFM was 0.1 nT; CHAMP's was 2 nT. The *Swarm* mission, launched in 2013, consists of three satellites (A, B, and C); A and B fly side by side at an altitude of 450 km; C flies higher, at 530 km. The orbital inclination of A and C is 87.35°; B's is 87.75°. Each satellite has a VFM, similar to CHAMP and Oersted, and an optically pumped scalar magnetometer.

The MSS-1 mission was launched on 21 May 2023 and orbits at an altitude of ~450 km. It is equipped with high-precision vector magnetometer and scalar magnetometer; it also has a non-magnetic stellar compass to determine the attitude of the magnetometer, and a highly stable optical bench, which serves as a platform for the VFM and the stellar compass. MSS-1A is unique in that its orbital angle is 41°, making its field measurements more sensitive to lateral variation, which is important for detecting North–South anomalies in the North Atlantic Ocean.

Observations of magnetic anomalies in the lithosphere exhibit a

Correspondence to: P. F. Liu, pengfei.liu2018@outlook.com
L. Yin, lyin@must.edu.mo
Received 17 FEB 2025; Accepted 31 MAR 2025.
First Published online 25 APR 2025.

wide spatial spectrum distribution that ranges from $O(10)$ km to $O(1000)$ km (Thébault et al., 2010; Zhang K, 2023). Short-wavelength scale magnetic structures, i.e., $O(10)$ km can hardly be probed by the current satellite observation at an altitude of more than 400 km, but satellite surveys are capable of capturing long-wavelength magnetic geological characteristics at both intermediate scale $O(100)$ km and large scale $O(1000)$ km. Currently, a number of geomagnetic field models have been derived from satellite data, magnetic observatories, and related data. These include the CM series (e.g. Sabaka et al., 2002), CHAOS series (e.g. Olsen et al., 2006; Finlay et al., 2020), POMME models (e.g. Maus et al., 2006), and GRIMM models (e.g. Lesur et al., 2008; Lesur et al., 2015) among others (e.g. Thomson and Lesur, 2007; Thomson et al., 2010; Yao HB et al., 2025a, b). As high-resolution data have accumulated, the CM series has been updated to its sixth-generation model, CM6 (Sabaka et al., 2002, 2020), and the CHAOS series has been updated from CHAOS-1 (Olsen et al., 2006) to CHAOS-7 (Finlay et al., 2020).

Some models concentrate only on the magnetic field that originates from the lithosphere (e.g. Maus et al., 2007; Stockmann et al., 2009; Kother et al., 2015; Thébault et al., 2016; Olsen et al., 2017; Wang J et al., 2023), of which the MF series has been updated from the first-generation MF1 (Maus et al., 2002) to the seventh-generation MF7 (Maus, 2010). A high-resolution lithospheric field model has been constructed by Olsen et al. (2017) based on gradient data derived from CHAMP and *Swarm* satellite observations, which has the advantage that the gradient data dampen large-scale signals that originate from magnetospheric currents (Olsen et al., 2017). Liu PF et al. (2023) showed that the intensity of the lithospheric magnetic field at an altitude of 400 km is between −14.8 nT and +18.2 nT at an altitude of 400 km, by employing the global vertically integrated magnetization (VIM) model, which uses a vector spherical harmonic method to resolve spherical harmonics up to degree $n = 256$ (Gubbins et al., 2011).

Here we present a preliminary study that focuses on modeling magnetic anomalies in the North Atlantic Ocean. We first construct a model that uses satellite measurements from the *Swarm* mission and then combine data from the MSS-1 satellite with *Swarm* data. We then compare the two models to evaluate how the addition of data from a satellite with low orbit contributes to anomaly resolution at the elevation of 450 km above the Earth's surface.

2. Magnetization of Oceanic Crust

The magnetization of the oceanic crust is dominated by remanent magnetization. The crust has a layered structure. The uppermost layer is composed of sediments; their magnetization is relatively weak, and thus negligible in satellite measurements. The second layer of the oceanic crust consists of basalt that is either extruded at the mid-oceanic ridge (upper basaltic layer) or as dikes that are intruded below the surface (lower basaltic layer). Extruded basalt cools more rapidly than the dikes, so the ferromagnetic mineralogy of the upper basaltic layer has a fine grain-size that is magnetized as it cools and retains a stable thermal remanent magnetization (TRM) that is stronger than that of the lower basalt of the dikes. The third layer of the crust is gabbroic. These rocks, also, can acquire a stable TRM, but because they cool more slowly, their ferromagnetic minerals have a coarser grain size and thus a weaker magnetization.

The Earth's magnetic field reverses many times through geological processes which leads to a magnetization in the opposite direction. This leads to an appearance of magnetic anomalies, parallel to the mid-oceanic ridge, exhibiting positive and negative magnetic amplitudes. The ferromagnetic minerals that are formed in the extruded basalts are known as *titanomagnetite* ($Fe_{3-x}Ti_xO_4$, with $x \approx 0.5$). The grains are not oxidized when extruded at the ridge, but undergo low-temperature oxidation with time (Wang DM et al., 2006) which alters the original mineral to a non-stoichiometric cation-deficient phase, $Fe_{3-x-z/3}Ti_x\square_{z/3}O_4$ through the oxidation of Fe(II) to Fe(III) and vacancy formation (Stacey and Banerjee, 1974). The amount of oxidation is characterized by z, which can range from 0 to 1.

That the magnetization intensity of rock specimens and the amplitude of magnetic anomalies in the ocean vary with the age of ocean crust has been known for decades (Johnson, 1979; Blakely, 1983; Bleil and Petersen, 1983). The magnetization intensity is highest in basalts between 20 Ma and 120 Ma in age; in older and younger basalts, intensity is lower (Bleil and Petersen, 1983). Magnetization varies also with depth, deeper rock exhibiting higher intensity (Kent et al., 1978; Dunlop and Prévot, 1982; Smith and Banerjee, 1986).

In this study, we focus on the North Atlantic Ocean area, which has an average age of 69.2 Ma, and exhibits a symmetrical spreading rate that averages around 20 mm/yr (Seton et al., 2020). Figure 1a displays the study's area — (90°W to 0°W, 0°N to 60°N) over the North Atlantic; Figure 1b shows the age distribution of this region of oceanic crust, revealing a lineated age pattern.

3. Method and Data

3.1 Model Parametrization

The magnetic potential U at point $\boldsymbol{r}'$ due to the magnetized materials in the lithosphere can be described (Blakely, 1995) as

$$U(\boldsymbol{r}') = \frac{-\mu_0}{4\pi}\int \boldsymbol{M}(\boldsymbol{r})\cdot\nabla'\frac{1}{|\boldsymbol{r}'-\boldsymbol{r}|}\mathrm{d}v = \frac{\mu_0}{4\pi}\int \boldsymbol{M}(\boldsymbol{r})\cdot\frac{\boldsymbol{r}'-\boldsymbol{r}}{|\boldsymbol{r}'-\boldsymbol{r}|^3}\mathrm{d}v, \quad (1)$$

where $U(\boldsymbol{r}')$ is magnetic potential, $\boldsymbol{r}'$ is the position of survey location, $\mu_0 = 4\pi\times10^{-7}$ N/A^2 is the permeability of free space, $\boldsymbol{M}(\boldsymbol{r})$is the magnetization vector distribution, $\boldsymbol{r}$ is the position of magnetization source dv, $\nabla'$is the gradient operator for observation coordinate $\boldsymbol{r}'$, and the integral is carried out over the magnetized region. The integral formula for the magnetic field $\boldsymbol{B}(\boldsymbol{r}')$ can be therefore written in the form

$$\boldsymbol{B}(\boldsymbol{r}') = -\nabla' U(\boldsymbol{r}') = \frac{\mu_0}{4\pi}\int\left(\frac{3\boldsymbol{M}\cdot\boldsymbol{R}}{R^5}\boldsymbol{R} - \frac{\boldsymbol{M}}{R^3}\right)\mathrm{d}v, \quad (2)$$

where $\boldsymbol{R} = \boldsymbol{r}' - \boldsymbol{r}$, and $R = |\boldsymbol{R}|$ is the L_2 norm of $\boldsymbol{R}$.

To integrate over the magnetized region, the lithosphere is approximated as a thin spherical shell and then discretized. In this study, a cubed-sphere grid method has been used to mesh the research area (Figure 2a). The cubed-sphere grid method is described in Yin L et al. (2017). For one cubed-sphere, the spherical

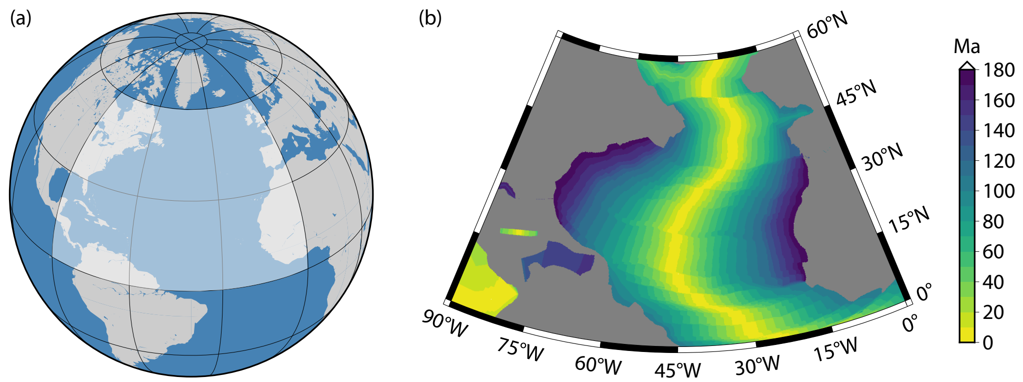

Figure 1. Study area overview. (a) Location of study area over the North Atlantic Ocean, and (b) oceanic crust age distribution, exhibiting a lineated pattern (Seton et al., 2020). Map view is centered on the 45°W meridian.

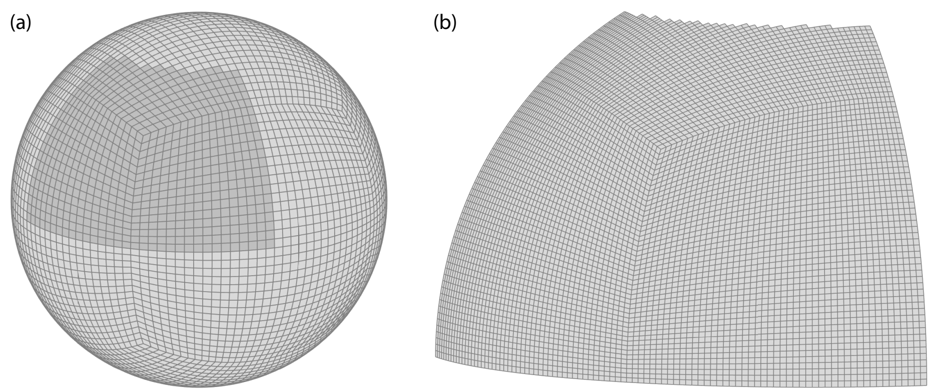

Figure 2. Illustration of the two-scale resolution cubed-sphere grids for a spherical shell. (a) A surface mesh with cubed-sphere grids, and dark grey highlights indicating the study region. (b) Refinement of the region of concern, with high-resolution grids.

surface is split into six patches with a local cubed-sphere coordinate employed for each patch. The entire spherical shell is analytically identified by combining the six partial coordinate systems. For more detailed information about the cubed-sphere grid technique, please see Yin L et al. (2017, 2025). The magnetic field by the discretized shell is described as

$$\boldsymbol{B}\left(\boldsymbol{r}'\right) = \frac{\mu_0}{4\pi}\sum_{i=1}^{N_{cs}}\int_i\left(\frac{3\boldsymbol{M}\cdot\boldsymbol{R}}{R^5}\boldsymbol{R} - \frac{\boldsymbol{M}}{R^3}\right)\mathrm{d}v = \sum_{i=1}^{N_{cs}}\boldsymbol{B}_i, \tag{3}$$

where $\boldsymbol{B}_i$ is the contribution of ith unit cell, and N_{cs} is the total number of meshed grid cells. The cubed-sphere grid has been refined over the research region (Figure 2b).

We assume that the magnetization vector is constant in each of the cubed-spherical grids. The magnetization direction is determined according to an improved global vertically-integrated remanent magnetization model (Sun SD et al., 2025). The magnetization intensity forms the model parameters. Using an equivalent source dipole method to calculate the cell contribution $\boldsymbol{B}_i$, the forward modeling is built and can be expressed in matrix form:

$$\boldsymbol{B}_e = \boldsymbol{G}_e\boldsymbol{m}, \tag{4}$$

where $\boldsymbol{B}_e$ is data column vector, the matrix $\boldsymbol{G}_e$ quantifies the contribution of unit cells to field datum, and $\boldsymbol{m} = \left[\lambda_1, \lambda_2, \cdots, \lambda_{N_{cs}}\right]^{\mathrm{T}}$ is the parameter vector in the cells.

3.2 Model Estimation

Model estimation is dealt with as an optimization problem. Following the inverse frame proposed by Li YG and Oldenburg (1996), the objective function is written as

$$\phi\left(\boldsymbol{m}\right) = \phi_d + \beta\phi_m, \tag{5}$$

where ϕ_d is the data misfit term, ϕ_m is the model regularization term, and β is the regularization parameter used to balance data residual and constraints of models. The data misfit term ϕ_d is expressed as

$$\phi_d = \sum_{k=1}^{K}\gamma_k\sum_{j=1}^{N_k}\left(\frac{d_{k,j}^{p} - d_{k,j}^{o}}{\varepsilon_{k,j}}\right)^2, \tag{6}$$

where K is the total number of data source kind, γ_k is the weight parameter of k-kind data, N_k is the total number of k-kind data, $d_{k,j}^{p}$ is model prediction, $d_{k,j}^{o}$ is observation value, and $\varepsilon_{k,j}$ is the weight of jth data misfit of k-kind data. The model regularization term is expressed as

$$\phi_m = \sum_{i=1}^{N_{cs}}\omega_i\left(m_i - m_i^{\mathrm{ref}}\right)^2, \tag{7}$$

where ω_i is the weight of ith unit cell, m_i is ith unit cell parameter, and m_i^{ref} is reference model value of ith unit cell. In this study, the reference model was set to a zero vector. To minimize the objective function, the optimization problem is transformed into the solution of a series of linear algebraic systems, which are solved by MATLAB direct solver. Uniform weights are used; the regularization parameter β is derived from the L-curve technique (Hansen, 1992).

3.3 Satellite Data

In this study, Swarm-A data from January 2014 to October 2024 with 1 Hz in Level-1b have been used, together with MSS-1 Level-2 data from November 2023 to October 2024, also using 1 Hz observations. Olsen (2025) compares the data between Swarm and MSS-1 and carries out a detailed joint analysis. Here we focus only on components of the magnetic field originating from the lithosphere; thus, observation features from other sources, such as the core field and magnetosphere, must be eliminated. Predictions of the CHAOS-7 model (Finlay et al., 2020) have been employed to remove the contribution from Earth's core and magnetosphere. The model built by Grayver and Olsen (2019) has been applied to remove the tidal magnetic influences.

4. Results

4.1 Local Magnetic Field Model

Figure 3 displays the amplitude of the oceanic crustal magnetic field at 450 km altitude derived from *Swarm* satellite data alone. There is a broad structure of positive and negative magnetic anomalies that lie parallel to the spreading ridge. The amplitudes of the radial magnetic field B_r range from −11.0 nT to +8.0 nT; B_θ amplitudes range from −6.5 nT to +6.9 nT; B_φ, from −6.2 nT to +5.0 nT. Note that the alternating magnetic stripes do not reflect all reversals of the Earth's magnetic field, due to the elevation of the satellite observations. The distribution of intensity of the anomalies is consistent with the sequence of oceanic crustal ages. The highest intensities are found in rocks that were extruded during the Cretaceous magnetic quiet zone, a long period of normal polarity from ca. 126 to 84 Ma.

Figure 4 displays the crust magnetic field distribution observed at 450 km altitude, derived from data provided by both MSS-1 and *Swarm* satellites. The amplitudes of the radial magnetic field B_r range from −11.1 nT to +8.0 nT; of B_θ the range is from −6.4 nT to +6.9 nT; and of B_φ, from −6.3 nT to +4.8 nT. The inversion model from the combined data set is similar to the model inverted from *Swarm* data alone, both with respect to the intensities and to the locations of the anomalies for all three components of the field. Differences between the models are presented in the following section.

4.2 Influence of MSS-1 Observation

To evaluate whether MSS-1 data have a significant effect on the reconstructed model of the crust's magnetic field, we calculated the differences between the above two results. Figure 5 displays

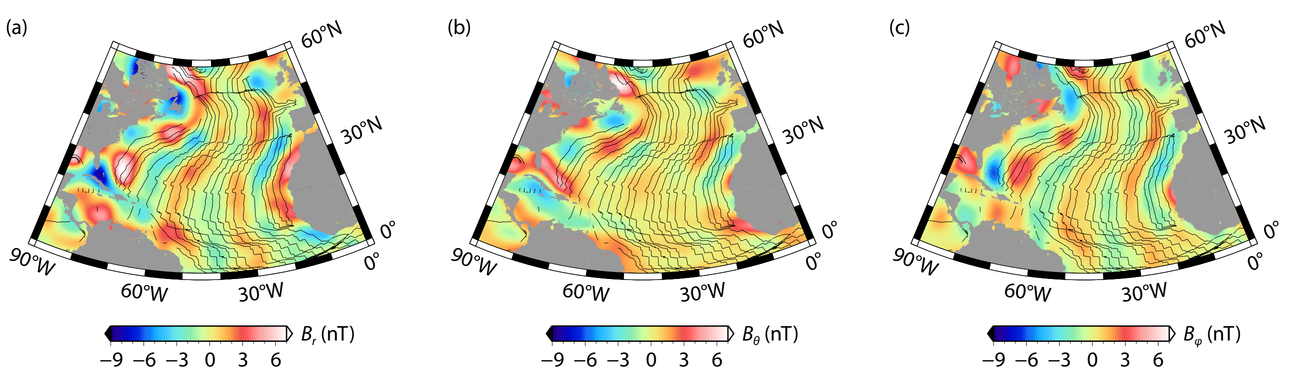

Figure 3. Maps of oceanic crust magnetic field observed at 450 km altitude. (a) Radial magnetic field (B_r), (b) B_θ component, and (c) B_φ component. The magnetic anomaly results shown were derived from *Swarm* satellite data. Map view is centered on the 45°W meridian; the gray lines indicate the oceanic crust age distribution.

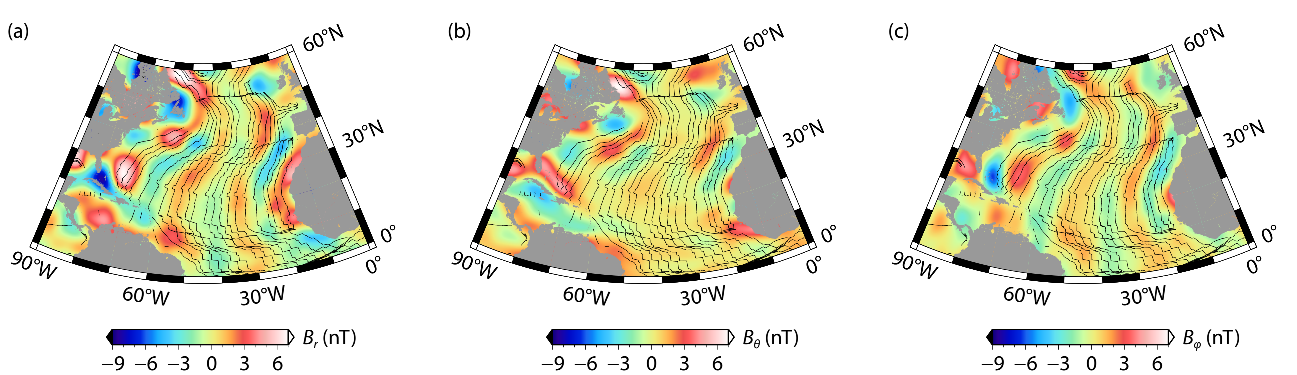

Figure 4. Maps of oceanic crust magnetic field distribution at 450 km altitude. (a) Vertical magnetic field (B_r), (b) B_θ component, and (c) B_φ component. The magnetic anomaly results presented here are derived from both MSS-1 and *Swarm* satellite data. Map view is centered on the 45°W meridian; the gray lines indicate the oceanic crust age pattern.

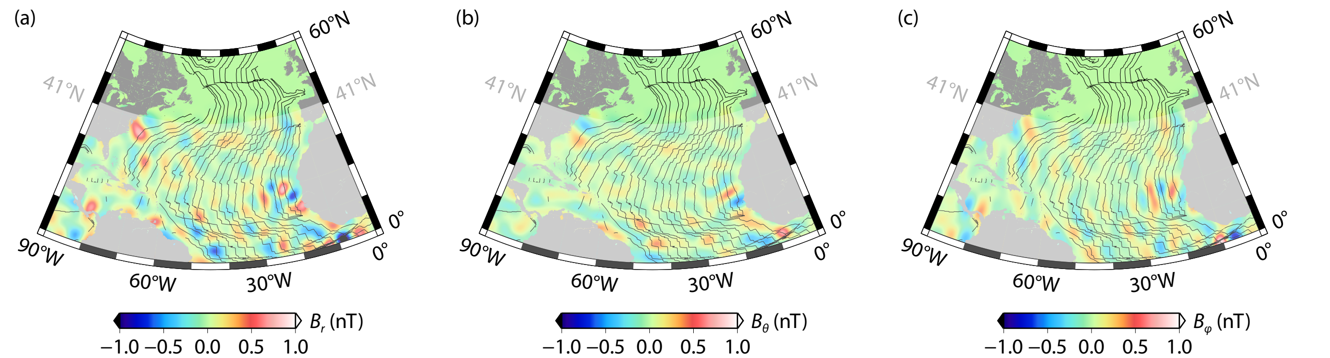

Figure 5. Residuals when the oceanic crust magnetic fields displayed in Figure 4 and Figure 3 are compared. (a) Vertical magnetic field (B_r) residuals; (b) B_θ component residuals; (c) B_φ component residuals. Map view is centered on the 45°W meridian; the gray lines indicate the oceanic crust age distribution; the lighter gray background between 0°N and 41° denote the MSS-1 data covering area, to which the comparison is limited.

the residual of the oceanic crust magnetic field derived from comprehensive data (*Swarm* + MSS-1) minus (*Swarm*) data alone. Note: Due to the difference in orbital inclination between the *Swarm* and MSS-1 satellites, we compared only latitudes ≤ 41°N.

The light gray shadow section between 0° and 41°N shows residuals that are significantly valid for the three components, B_r, B_θ, and B_φ. The largest residuals tend to be found in areas between large anomalies along the east coast of the USA, or along the west coast of Northern Africa in the oldest, thus higher intensity, crustal rocks. Larger residuals are found also in the equatorial zone.

5. Discussion

Modeling the Earth's magnetic field, based on data collected by the *Swarm* and MSS-1 satellites, demonstrates that it is possible to resolve, from space observations, a pattern of magnetic anomalies with opposite polarity in the oceanic crust in the North Atlantic Ocean, and that the observed pattern reflects the known symmetry of mid-oceanic spreading ridges. Furthermore, the difference in the intensity of the anomalies as a function of age is also seen in the model. During the first 40 ka, there is a decrease in the intensity of the natural remanent magnetization by a factor of 4 when moving away from the ridge (Gee and Kent, 2007). This pattern can be explained by low-temperature oxidation of the original titanomagnetite, which leads to vacancy diffusion, caused by stress, and crack formation that affects the domain structure of the original coarse-grained ferromagnetic mineral (Fabian and Shcherbakov, 2020). The increase in intensity that was observed by (Bleil and Petersen, 1983) is also seen in the oldest crust, where the anomalies are the strongest.

We find that incorporation of magnetic field observations from the MSS-1 into *Swarm* data does not alter the overall pattern of anomalies. Analysis of residual results, however, suggests that data from the MSS-1 mission, with its lower orbital inclination, may provide more information on the anomaly structure (Figure 5). Recent studies demonstrate the value of MSS-1 surveys (e.g., Williams et al., 2025; Ren ZY et al., 2025; Feng Y et al., 2025). Note that the measurement precision of the MSS-1 is superior to 0.5 nT, which is on the order of the residuals. However, the largest residual exceeds the precision of the measurements, which may be useful in refining structures.

Our analysis demonstrates, however, that it is not possible to resolve anomalies of individual polarities, due to the cubic attenuation of the potential of the signal as a function of distance. Due to the high altitude of current satellite observations, satellite data alone are insufficient to delineate any fine structure of oceanic magnetic stripes. Detection of short-wavelength features, such as individual polarities, can be obtained only by incorporating magnetic field measurements that are collected closer to the surface of the Earth, such as aeromagnetic surveys, marine magnetic surveys, and observatory surveys.

Refining the pattern of magnetic anomalies that are recorded in Earth's crust can provide important fingerprints in untangling the evolutionary history of geomagnetic polar reversals, geomagnetic excursions, seafloor spreading, and plate motion. Betts et al. (2024) have thoroughly discussed the gap between knowledge of geologic features and interpretations derived from aeromagnetic data; the same problem is valid for higher-altitude satellite magnetic measurements. High-precision observation or lack thereof has a strong influence on the reconstruction of reliable geomagnetic field models. Satellite observations are important because they provide a more homogenous coverage of the Earth; when combined with ground, marine, and aeromagnetic measurements, satellite data will allow creation of more precise models of the Earth's field.

6. Conclusions

This preliminary study illustrates the resolution that can be obtained when combining magnetic field measurements from MSS-1 and *Swarm* satellites, using an equivalent source dipole method based on cubed-sphere grid. Based on satellite data alone, we have obtained a pattern of magnetic anomalies with alternating opposite polarities over the North Atlantic Ocean. The pattern of anomalies we present here is consistent with the oceanic crust age frame pattern. Our model indicates that data collected in the low-inclination orbit of MSS-1 can resolve the east–west variation in the magnetic field. In the future, gradient data will be available from MSS-1 that can be applied to refine, significantly, oceanic crust magnetic field models. Further refinement of our understanding of the structure of oceanic anomalies can be obtained with this new data set, by combining the MSS-1 satellite observations with near-surface magnetic data.

Acknowledgments

This research is supported by the National Natural Science Foundation of China (42250101, 42250102,42250103), the Macau Foundation, and the Science and Technology Development Fund, Macau SAR (File No. 0002/2019/APD). CNSA and ESA are gratefully acknowledged for their support. We thank A. M. Hirt for her critical feedback and suggestions.

Author contributions

The research has been designed by PL and LY, and carried out by PL, LY, SS, and HY. All authors were involved in writing the text, and have seen the final version. The manuscript has not been submitted to another journal and there are no conflicts of interest.

References

Betts, P. G., Moore, D., Aitken, A., Blaikie, T., Jessell, M., Ailleres, L., Armit, R., McLean, M., Munukutla, R., and Chukwu, C. (2024). Geology from aeromagnetic data. *Earth-Sci. Rev.*, *258*, 104958. https://doi.org/10.1016/j.earscirev.2024.104958

Blakely, R. J. (1983). Statistical averaging of marine magnetic anomalies and the aging of oceanic crust. *J. Geophys. Res.: Solid Earth*, *88*(B3), 2289–2296. https://doi.org/10.1029/JB088iB03p02289

Blakely, R. J. (1995). *Potential Theory in Gravity and Magnetic Applications*. Cambridge: Cambridge University Press. https://doi.org/10.1017/CBO9780511549816

Bleil, U., and Petersen, N. (1983). Variations in magnetization intensity and low-temperature titanomagnetite oxidation of ocean floor basalts. *Nature*, *301*(5899), 384–388. https://doi.org/10.1038/301384a0

Dunlop, D. J., and Prévot, M. (1982). Magnetic properties and opaque mineralogy of drilled submarine intrusive rocks. *Geophys. J. Int.*, *69*(3), 763–802. https://doi.org/10.1111/j.1365-246X.1982.tb02774.x

Ebbing, J., Dilixiati, Y., Haas, P., Ferraccioli, F., and Scheiber-Enslin, S. (2021). East Antarctica magnetically linked to its ancient neighbours in Gondwana. *Sci. Rep.*, *11*(1), 5513. https://doi.org/10.1038/s41598-021-84834-1

Fabian, K., and Shcherbakov, V. P. (2020). The magnetization of the ocean floor: stress and fracturing of titanomagnetite particles by low-temperature oxidation. *Geophys. J. Int.*, *221*(3), 2104–2112. https://doi.org/10.1093/gji/ggaa142

Feng, Y., Li, X. W., Lin, Y. X., Zhang, J. X., Zhang, J. Y., Jiang, Y., Yan, Q., and Liu, P. F. (2025). Utilising macau science Satellite-1 data and comprehensive datasets to develop a lithospheric magnetic field model of the Chinese Mainland. *Remote Sensing*, *17*(7), 1114. https://doi.org/10.3390/rs17071114

Finlay, C. C., Kloss, C., Olsen, N., Hammer, M. D., Tøffner-Clausen, L., Grayver, A., and Kuvshinov, A. (2020). The CHAOS-7 geomagnetic field model and observed changes in the South Atlantic Anomaly. *Earth Planets Space*, *72*(1), 156. https://doi.org/10.1186/s40623-020-01252-9

Gee, J. S., and Kent, D. V. (2007). Source of oceanic magnetic anomalies and the geomagnetic polarity timescale. In G. Schubert (Ed.), *Treatise on Geophysics* (Vol. 5, pp. 455-507). Amsterdam: Elsevier. https://doi.org/10.1016/B978-044452748-6.00097-3

Grayver, A. V., and Olsen, N. (2019). The magnetic signatures of the M_2, N_2, and O_1 oceanic tides observed in Swarm and CHAMP satellite magnetic data. *Geophys. Res. Lett.*, *46*(8), 4230–4238. https://doi.org/10.1029/2019GL082400

Gubbins, D., Ivers, D., Masterton, S. M., and Winch, D. E. (2011). Analysis of lithospheric magnetization in vector spherical harmonics. *Geophys. J. Int.*, *187*(1), 99–117. https://doi.org/10.1111/j.1365-246X.2011.05153.x

Hansen, P. C. (1992). Analysis of discrete ill-posed problems by means of the L-curve. *SIAM Rev.*, *34*(4), 561–580. https://doi.org/10.1137/1034115

Johnson, H. P. (1979). Magnetization of the oceanic crust. *Rev. Geophys.*, *17*(2), 215–226. https://doi.org/10.1029/RG017i002p00215

Kent, D. V., Honnorez, B. M., Opdyke, N. D., and Fox, P. J. (1978). Magnetic properties of dredged oceanic gabbros and the source of marine magnetic anomalies. *Geophys. J. Int.*, *55*(3), 513–537. https://doi.org/10.1111/j.1365-246X.1978.tb05925.x

Kother, L., Hammer, M. D., Finlay, C. C., and Olsen, N. (2015). An equivalent source method for modelling the global lithospheric magnetic field. *Geophys. J. Int.*, *203*(1), 553–566. https://doi.org/10.1093/gji/ggv317

Lesur, V., Wardinski, I., Rother, M., and Mandea, M. (2008). GRIMM: The GFZ Reference Internal Magnetic Model based on vector satellite and observatory data. *Geophys. J. Int.*, *173*(2), 382–394. https://doi.org/10.1111/j.1365-246X.2008.03724.x

Lesur, V., Rother, M., Wardinski, I., Schachtschneider, R., Hamoudi, M., and Chambodut, A. (2015). Parent magnetic field models for the IGRF-12GFZ-candidates. *Earth Planets Space*, *67*(1), 87. https://doi.org/10.1186/s40623-015-0239-6

Li, Y. G., and Oldenburg, D. W. (1996). 3-D inversion of magnetic data. *Geophysics*, *61*(2), 394–408. https://doi.org/10.1190/1.1443968

Liu, P. F., Jiang, Y., Yan, Q., and Hirt, A. M. (2023). The behavior of a lithospheric magnetization and magnetic field model. *Earth Planet. Phys.*, *7*(1), 66–73. https://doi.org/10.26464/epp2023025

Maus, S., Rother, M., Holme, R., Lühr, H., Olsen, N., and Haak, V. (2002). First scalar magnetic anomaly map from CHAMP satellite data indicates weak lithospheric field. *Geophys. Res. Lett.*, *29*(14), 45–1-47-4. https://doi.org/10.1029/2001GL013685

Maus, S., Rother, M., Stolle, C., Mai, W., Choi, S., Lühr, H., Cooke, D., and Roth, C. (2006). Third generation of the Potsdam Magnetic Model of the Earth (POMME). *Geochem. Geophys. Geosyst.*, *7*(7), Q07008. https://doi.org/10.1029/2006GC001269

Maus, S., Lühr, H., Rother, M., Hemant, K., Balasis, G., Ritter, P., and Stolle, C. (2007). Fifth-generation lithospheric magnetic field model from CHAMP satellite measurements. *Geochem. Geophys. Geosyst.*, *8*(5), Q05013. https://doi.org/10.1029/2006GC001521

Maus, S. (2010). Magnetic field model MF7. https://www.geomag.us/models/MF7.html

Olsen, N., Lühr, H., Sabaka, T. J., Mandea, M., Rother, M., Tøffner-Clausen, L., and Choi, S. (2006). CHAOS — a model of the Earth's magnetic field derived from CHAMP, Ørsted, and SAC-C magnetic satellite data. *Geophys. J. Int.*, *166*(1), 67–75. https://doi.org/10.1111/j.1365-246X.2006.02959.x

Olsen, N., Ravat, D., Finlay, C. C., and Kother, L. K. (2017). LCS-1: a high-resolution global model of the lithospheric magnetic field derived from CHAMP and *Swarm* satellite observations. *Geophys. J. Int.*, *211*(3), 1461–1477. https://doi.org/10.1093/gji/ggx381

Olsen, N. (2025). Combining polar-orbiting and low-inclination satellites — Joint analysis of data from MSS-1 and *Swarm*. *Earth Planet. Phys.*, *9*(3), 500–510. https://doi.org/10.26464/epp2025024

Ren, Z. Y., Huang, Y. P., Yang, C., Chen, C. J., and Zhang, K. (2025). Preliminary results suggest observations from Macau Science Satellite-1 system can improve knowledge of tidal-induced magnetic fields. *Earth Planet. Phys.*, *9*(3), 586–594. https://doi.org/10.26464/epp2025002

Sabaka, T. J., Olsen, N., and Langel, R. A. (2002). A comprehensive model of the quiet-time, near-Earth magnetic field: phase 3. *Geophys. J. Int.*, *151*(1), 32–68. https://doi.org/10.1046/j.1365-246X.2002.01774.x

Sabaka, T. J., Tøffner-Clausen, L., Olsen, N., and Finlay, C. C. (2020). CM6: a comprehensive geomagnetic field model derived from both CHAMP and Swarm satellite observations. *Earth Planets Space*, *72*(1), 80. https://doi.org/10.1186/s40623-020-01210-5

Seton, M., Müller, R. D., Zahirovic, S., Williams, S., Wright, N. M., Cannon, J., Whittaker, J. M., Matthews, K. J., and McGirr, R. (2020). A global data set of present-day oceanic crustal age and seafloor spreading parameters. *Geochem. Geophys. Geosyst.*, *21*(10), e2020GC009214. https://doi.org/10.1029/2020GC009214

Smith, G. M., and Banerjee, S. K. (1986). Magnetic structure of the upper kilometer of the marine crust at Deep Sea Drilling Project Hole 504B, eastern Pacific Ocean. *J. Geophys. Res.: Solid Earth*, *91*(B10), 10337–10354. https://doi.org/10.1029/JB091iB10p10337

Stacey, F. D., and Banerjee, S. K. (1974). *The Physical Principles of Rock Magnetism*. Amsterdam: Elsevier.

Stockmann, R., Finlay, C. C., and Jackson, A. (2009). Imaging Earth's crustal magnetic field with satellite data: a regularized spherical triangle tessellation approach. *Geophys. J. Int.*, *179*(2), 929–944. https://doi.org/10.1111/j.1365-246X.2009.04345.x

Sun, S. D., Li, H., Du, J. S., Zhang, P., Chen, C., and Liu, P. F. (2025). Revised global vertically integrated remanent magnetization model of the oceanic lithosphere with comparison to LCS-1 model and MSS-1 magnetic measurements. *Earth Planet. Phys.*, *9*(3), 653–666. https://doi.org/10.26464/epp2025032

Thébault, E., Purucker, M., Whaler, K. A., Langlais, B., and Sabaka, T. J. (2010). The magnetic field of the Earth's lithosphere. *Space Sci. Rev.*, *155*(1), 95–127. https://doi.org/10.1007/s11214-010-9667-6

Thébault, E., Vigneron, P., Langlais, B., and Hulot, G. (2016). A Swarm lithospheric magnetic field model to SH degree 80. *Earth Planets Space, 68*(1), 126. https://doi.org/10.1186/s40623-016-0510-5

Thomson, A. W. P., and Lesur, V. (2007). An improved geomagnetic data selection algorithm for global geomagnetic field modelling. *Geophys. J. Int.*, *169*(3), 951–963. https://doi.org/10.1111/j.1365-246X.2007.03354.x

Thomson, A. W. P., Hamilton, B., Macmillan, S., and Reay, S. J. (2010). A novel weighting method for satellite magnetic data and a new global magnetic field model. *Geophys. J. Int.*, *181*(1), 250–260. https://doi.org/10.1111/j.1365-246X.2010.04510.x

Wang, D. M., Van der Voo, R., and Peacor, D. R. (2006). Low-temperature alteration and magnetic changes of variably altered pillow basalts. *Geophys. J. Int.*, *164*(1), 25–35. https://doi.org/10.1111/j.1365-246X.2005.02819.x

Wang, J., Shen, X. H., Yang, Y. Y., Zeren, Z. M., Zhou, B., Werner, M., De Santis, A., Huang, J. P., Yao, C. L., … Lammegger, R. (2023). A global lithospheric magnetic field model between ± 65° latitude derived from CSES satellite scalar data. *Phys. Earth Planet. Inter.*, *340*, 107036. https://doi.org/10.1016/j.pepi.2023.107036

Williams, S., Gubbins, D., Livermore, P. W., and Jiang, Y. (2025). Evaluation of the lithospheric magnetic field mapped by the first year of MSS-1 data. *Earth Planet. Phys.*, *9*(3), 614–621. https://doi.org/10.26464/epp2025033

Yao, H. B., Xu, J. Y., Jiang, Y., Yan, Q., Yin, L., and Liu, P. F. (2025a). Influence of different data selection criteria on internal geomagnetic field modeling. *Earth Planet. Phys.*, *9*(3), 541–549. https://doi.org/10.26464/epp2025013

Yao, H. B., Xu, J. Y., and Zhang, K. (2025b). A method for simultaneously determining Earth's magnetic field and mantle conductivity models using MSS-1 and Swarm satellite magnetic data. *Phys. Earth Planet. Inter.*, *358*, 107296. https://doi.org/10.1016/j.pepi.2024.107296

Yin, L., Yang, C., Ma, S. Z., Huang, J. Z., and Cai, Y. (2017). Parallel numerical simulation of the thermal convection in the Earth's outer core on the cubed-sphere. *Geophys. J. Int.*, *209*(3), 1934–1954. https://doi.org/10.1093/gji/ggx125

Yin, L., Zhang, J. X., Liu, P. F., Yao, H. B., Zhang, P., and Du, J. S. (2025). A cubed-sphere based method for global and regionalmodeling of the lithospheric magnetic field. *Earth Planet. Phys*, *9*(3), 622–634. https://doi.org/10.26464/epp2025064

Zhang, K. (2023). A novel geomagnetic satellite constellation: science and applications. *Earth Planet. Phys.*, *7*(1), 4–21. https://doi.org/10.26464/epp2023019